JACS
JOURNAL OF THE AMERICAN CHEMICAL SOCIETY
pubs.acs.org/JACS

Article

Quantum Interference in a Molecular Analog of the Crystalline Silicon Unit Cell

Matthew O. Hight,[⊥] Ashley E. Pimentel,[⊥] Timothy C. Siu, Joshua Y. Wong, Jennifer Nguyen, Veronica Carta, and Timothy A. Su*

Cite This: J. Am. Chem. Soc. 2025, 147, 16602−16610

Read Online

ACCESS | Metrics & More | Article Recommendations | Supporting Information

ABSTRACT: This manuscript describes the emergence of destructive σ-quantum interference (σ-DQI) in sila-adamantane, a molecule whose cluster core is isostructural with the crystalline silicon unit cell. To reveal these σ-DQI effects, we take a bridge-cutting approach where we conceptually pare sila-adamantane down to its bicyclic Si[3.3.1] and linear oligosilane forms. Scanning tunneling microscopy break-junction (STM-BJ) measurements reveal that conductance in single-molecule junctions of the tricyclic sila-adamantane is 2.7-times lower than their bicyclic Si[3.3.1] analog. The only structural difference between their cluster cores is a remote dimethylsilylene bridge that is present in sila-adamantane yet absent in Si[3.3.1]. Density functional theory calculations reveal that this dimethylsilylene enforces C_3 symmetry at the sila-diamondoid bridgeheads, allowing each electrode to couple into the three cluster bridge dimensions equally. Though each bridge alignment is sterically equivalent, they have profound electronic differences: when electrodes align with the long branches of sila-adamantane, strong σ-DQI interactions occur between frontier molecular orbitals that suppress electronic transmission across the molecular junction. We exploit these alignment-dependent σ-DQI effects to create new forms of stereoelectronic conductance switches, where a reversible mechanical stimulus controls which pathway through the diamondoid framework the electrodes align through. This represents the first example of dynamic modulation of σ-DQI and enables us to achieve switching ratios (average on/off ∼5.6) higher than previously reported σ-stereoelectronic switches. These studies reveal how the innate dimensionality and symmetry of crystalline silicon influence charge transport at its most fundamental level, and how these principles can be harnessed to control quantum interference in single-molecule electronics.

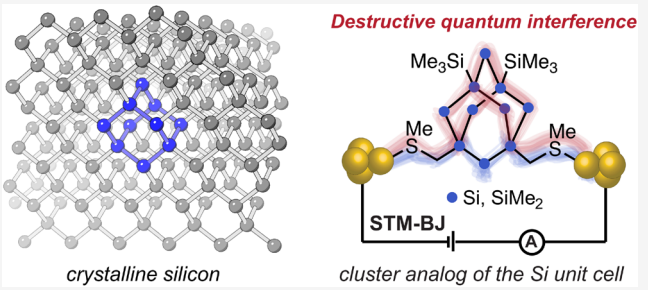

INTRODUCTION

Here we describe the structural origins of quantum interference effects that we find dictate charge transport in single-molecule junctions of sila-adamantane, the smallest form of crystalline silicon. The miniaturization of crystalline silicon (Figure 1a) semiconductors has driven the major advancements in modern computing over the past few decades, with minimum transistor feature sizes now in the single-nanometer regime.[1−3] As silicon electronics continue to miniaturize, it is more important than ever to understand the factors that dictate charge transport in silicon at molecular length scales, where quantum tunneling becomes the dominant transport mechanism. Indeed, quantum tunneling in crystalline silicon has already presented itself as both a challenge and opportunity in advanced computing technologies. In modern field-effect transistors, quantum transport through silicon is an obstacle, where tunneling between the silicon channel and gate through the oxide creates leakage currents that reduce device efficiency.[2,4] Meanwhile silicon spin qubits exploit tunable tunnel coupling between single electrons in silicon quantum dots to execute quantum computing operations.[5,6] It is then crucial for us to understand how quantum tunneling occurs through crystalline silicon at its most basic level, as it will more deeply inform how quantum transport through silicon may be harnessed and controlled.

These interests have motivated recent work studying quantum transport through Si−Si σ-bonds in linear and multicyclic polysilane backbones.[7−9] A motivating factor in these studies has been to trace the origins of silicon semiconductor electronics back to their fundamental molecular forms. Scanning tunneling microscopy break-junction (STM-BJ)[10,11] studies first revealed that *anti*-like Si−Si bond arrangements are significantly more transmissive than C−C ones, mirroring conductivity trends between bulk silicon and carbon.[12,13] Next, quantum transport through multicyclic Si

Received: March 11, 2025
Revised: April 22, 2025
Accepted: April 23, 2025
Published: May 1, 2025

https://doi.org/10.1021/jacs.5c04272
J. Am. Chem. Soc. 2025, 147, 16602−16610

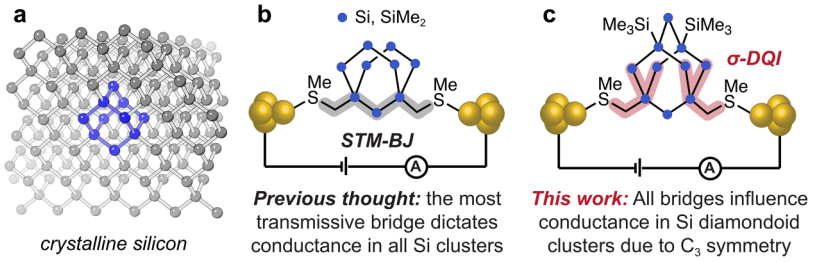

Figure 1. (a) Si diamondoids are isostructural with the diamond cubic unit cell (blue) of crystalline silicon. (b) Previous STM-BJ studies suggest that multicyclic Si clusters in single-molecule junctions behave as constrained linear oligosilanes, where transport is dominated by the most transmissive linear path of the cluster. The Si[3.3.1] cluster depicted is novel to this study. (c) This work shows that the C_3 bridgehead symmetry of sila-adamantane allows Au electrode (gold spheres) alignment with all cluster bridge paths of the diamondoid framework. For the sila-adamantane investigated herein, alignment with the long bridge paths leads to pronounced destructive σ-quantum interference (σ-DQI) effects.

clusters was measured, partially out of a curiosity to understand the extent to which the multiple branching paths of σ-delocalized clusters contribute to transmission.[14−17] These studies found that charge transport through bicyclic Si cluster junctions can be described as being akin to transport through a constrained linear polysilane, where the branching paths of the cluster do not meaningfully influence transport beyond structurally locking the most transmissive linear path of the cluster in place (Figure 1b).[16] This finding is notable because it does not mirror bulk trends. Indeed, crystalline silicon cannot be conceived simply as a constrained polysilane: the dimensionality and symmetry of three-dimensional crystalline silicon endow it with band structure characteristics and properties that are markedly distinct from one-dimensional polysilane.[18] This breakdown led us to wonder whether the structural nuances of bulk silicon were appropriately captured in previous STM-BJ studies on multicyclic Si wires, as none of the investigated clusters were true homologues of crystalline silicon.

Sila-adamantane, first isolated by Marschner and co-workers in 2005,[19] is a molecular silicon cluster whose core is identical in structure to the diamond cubic unit cell of silicon. It thus represents the ultimate limit of physical miniaturization for crystalline silicon, and in our view, an ideal model system for probing how the diamond structure of silicon influences charge transport at an atomically exact level. We recently reported synthetic approaches to control the peripheral structure of sila-adamantane that enable its connection to electrodes (Figure 1c).[20,21] These capabilities allow us now to consider: (1) will sila-adamantane follow the prescription for previous bicyclic Si clusters and behave as a constrained linear Si_3 wire? (2) Is there anything defining about its diamond structure that electronically distinguishes it from other Si clusters?

To answer these questions, we conceived of a "bridge-cutting" approach, where we conceptually pare the connective bridge paths in the tricyclic **SiAd** down to its bicyclic **Si**[**3.3.1**] analog, then to linear $\mathbf{Si_3}$ (Figure 2a). If these multicyclic wires behaved as analogs of constrained linear Si_3, we would expect their single-molecule conductance to be roughly equivalent due to the distance-dependent nature of tunneling transport (Figure S1).[22] Ultimately, this manuscript finds that this is not the case: single-molecule conductance through **SiAd** is significantly lower due to strong destructive σ-quantum interference effects[15] that occur when electrodes *anti*-align with the long bridging paths of the diamond framework. These findings suggest that the three-dimensional bridge paths and C_3 symmetry inherent to the diamond structure influence transport regardless of linker group identity, representing a marked departure from the single-molecule electronic behavior of polysilane and bicyclic cluster wires.

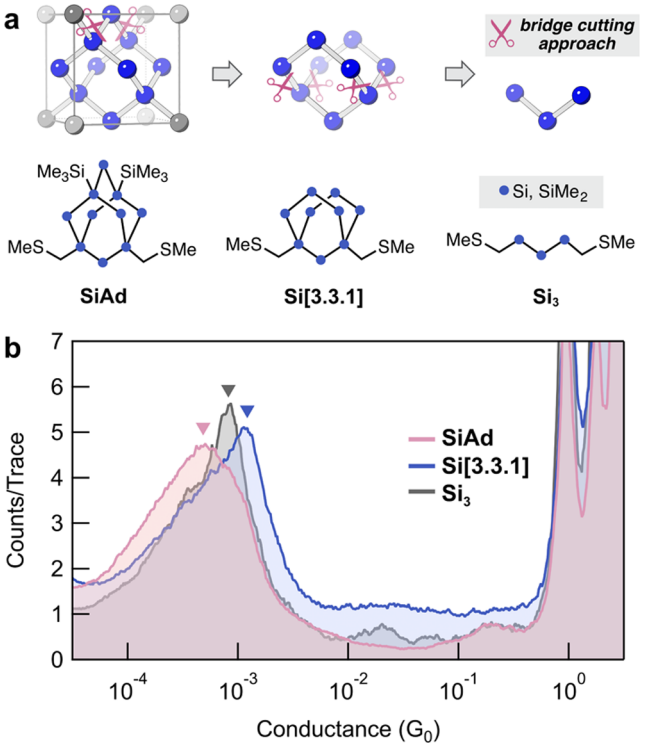

Figure 2. (a) "Bridge-cutting approach" to explore the role of connective paths from tricyclic **SiAd** to bicyclic **Si**[**3.3.1**] to linear $\mathbf{Si_3}$. All molecules in the series share a common trisilane bridge between methylthiomethyl linker groups. (b) Overlaid 1D conductance histograms of **SiAd** (pink), **Si**[**3.3.1**] (blue), and $\mathbf{Si_3}$ (gray) that compile 10,000 measurement traces for each molecule. All molecules were measured in 1 mM solutions in 1,2,4-trichlorobenzene at 0.1 V bias. Most probable conductance peaks are marked by triangles and their values are **SiAd** (4.4×10^{-4} G_0), **Si**[**3.3.1**] (1.2×10^{-3} G_0), $\mathbf{Si_3}$ (8.1×10^{-4} G_0).

RESULTS AND DISCUSSION

SiAd and $\mathbf{Si_3}$ (Figure 2a) were synthesized according to previous methods.[13,20] **Si**[**3.3.1**] is a novel compound that we made from reacting Marschner's Si[3.3.1] cluster dianion[23] with chloromethyl methyl sulfide (Scheme S1). With these molecular wires in hand, we measured conductance across single-molecule junctions of **SiAd**, **Si**[**3.3.1**], and $\mathbf{Si_3}$ using the

https://doi.org/10.1021/jacs.5c04272
J. Am. Chem. Soc. 2025, 147, 16602−16610

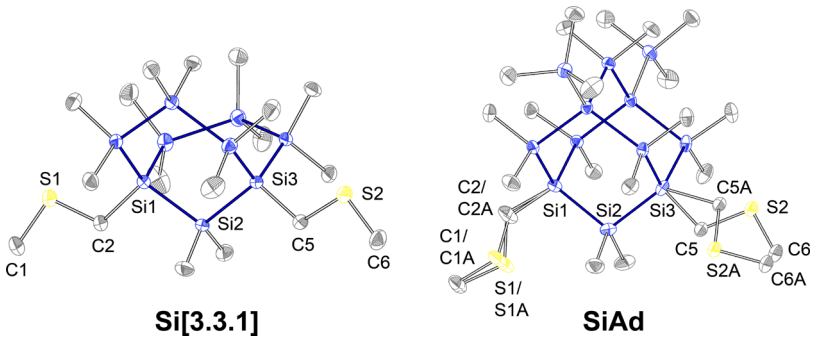

Figure 3. Molecular structures of **Si**[**3.3.1**] (left) and **SiAd** (right) determined via single-crystal X-ray diffraction with disorder included. While the S−C−Si−Si dihedrals in **Si**[**3.3.1**] are anti-like, the same dihedrals in **SiAd** possess significantly more gauche character (1). Thermal ellipsoids are plotted at 50% probability. Hydrogen atoms omitted for clarity. Atoms are colored gray (C), blue (Si), yellow (S).

STM-BJ technique described previously (see Supporting Information for more detail).[10,11]

In brief, the measurement setup is a two-electrode system with a gold STM tip-electrode attached to a piezoelectric motor and a gold substrate electrode. A dilute solution (1 mM) of the molecular wire in 1,2,4-trichlorobenzene is dropped onto the substrate. The STM tip and substrate are then brought into contact, after which the STM tip is pulled away. As the STM tip is retracted, the electrode contact is thinned to a single Au−Au point contact. The conductance of this point contact, G_0 (~77 μS), represents our basic unit of conductance. Once the point contact breaks, a single-molecule junction forms, where the molecules in solution bridge both electrodes by donor−acceptor bonding between thioether end groups and gold. Current is measured through the junction as the interelectrode distance increases until the Au-molecule-Au junction eventually ruptures, thus completing a single measurement trace. At least ten thousand conductance traces are acquired for each molecule. These traces are compiled into 1D histograms (Figure 2b and Figure S2) that allow us to extract the most probable conductance of each molecule. 2D histograms are also generated that relate conductance data with electrode displacement distance (Figure S3).[24] We note the 1D histograms for each molecule show overlapping conductance peak features. Figure S2 shows these features are reproducible across experiments. Their molecular origins will be addressed later in the manuscript.

The molecular wires in Figure 2 allow us to evaluate the influence of cluster branches at the 1,3-positions of the common trisilane chain. First, we find that molecular junctions of **Si**[**3.3.1**] are 1.5-fold higher in conductance than $\mathbf{Si_3}$ when comparing their peak values. The higher conductance observed for the bicyclic wire is consistent with previous conclusions that bicyclic silanes may be conceived as constrained linear systems in molecular conductance contexts (Figure 1b). We note that the most probable conductance peak value of the novel **Si**[**3.3.1**] is the same as the previously measured **Si**[**2.2.1**] (1.2×10^{-3} G_0), a cluster that is similar in structure to **Si**[**3.3.1**] but contains disilane rather than trisilane bridging arms.[16] Whereas the dihedral (ω) of the C−Si−Si−Si backbone in $\mathbf{Si_3}$ is flexible with transoid ($\omega \sim \pm 165°$)[1] energy minima, the bicyclic **Si**[**3.3.1**] is rigid with fixed backbone dihedrals approaching *anti* geometries ($\omega = 180°$, Figure 3). As oligosilane dihedrals approach the *anti* limit, HOMO destabilization and coupling between the S pπ lone pair orbitals are maximized.[13,25−28] Both factors increase charge transmission and contribute to **Si**[**3.3.1**] having a higher conductance than linear $\mathbf{Si_3}$. However, this logic does not follow for **SiAd**.

Like **Si**[**3.3.1**], **SiAd** has rigid *anti*-like dihedrals in its trisilane short path. Their dihedral angle (Figure 3 and Table 1) and bond angle (Table S1) similarities are apparent from their single-crystal X-ray diffraction (SCXRD) structures. Yet molecular junctions of **SiAd** are lower in conductance by 2.7-fold (Figure 2b). The only structural difference between their cluster cores is that **SiAd** contains a single dimethylsilylene unit that tethers the pendant cyclohexasilane rings of the **Si**[**3.3.1**] structure together (Figures 2a and 3). This single-atom bridge is physically remote from the trisilane short path, yet it significantly attenuates quantum transport compared to its bicyclic **Si**[**3.3.1**] congener. We were eager to understand this notion more deeply, as it suggests an atom-level explanation for how the diamond structure of crystalline

Table 1. Dihedral Angles Determined from SCXRD Structures Along the Trisilane Short Bridge in Si[**3.3.1**] **and SiAd**

Dihedral (ω)	Si[3.3.1]	SiAd
C1-S1-C2-Si1	-173.9(1)°	176.5(5)°
C1A-S1A-C2A-Si1[a]	——	-177(2)°
S1-C2-Si1-Si2[b]	173.97(8)°	-48.0(6)°
S1A-C2A-Si1-Si2	——	-25(2)°
C2-Si1-Si2-Si3	-173.20(6)°	-178.0(3)°
C2A-Si1-Si2-Si3	——	-178(1)°
Si1-Si2-Si3-C5	176.85(7)°	-176.62(6)°
Si1-Si2-Si3-C5A	——	170.5(6)°
Si2-Si3-C5-S2	-177.89(8)°	-167.10(8)°
Si2-Si3-C5A-S2A	——	46.1(9)°
Si3-C5-S2-C6	177.6(1)°	-171.0(1)°
Si3-C5A-S2A-C6A	——	-178(1)°

[a]The methylthiomethyl linker atoms are disordered in SiAd, giving rise to two distinct dihedral sets. [b]S−C−Si−Si (linker-cluster) torsion angles are highlighted in gray.

https://doi.org/10.1021/jacs.5c04272
J. Am. Chem. Soc. 2025, 147, 16602−16610

silicon fundamentally changes its charge transport properties compared to polysilanes at large.

Differences in the disorder and geometry of the methylthiomethyl linker dihedrals in the **Si**[**3.3.1**] and **SiAd** SCXRD structures provide the first clue for how the dimethylsilylene bridge in **SiAd** induces such a strong influence on conductance. The S−C−Si−Si dihedrals are *anti* for **Si**[**3.3.1**], yet disordered for **SiAd** with significant *gauche* character in both linker arms (Figure 3). These differences suggest a much weaker energetic preference for *anti* S−C−Si−Si dihedral conformations in **SiAd** compared to **Si**[**3.3.1**]. If this were the case, it would strongly influence transmission: in linear oligosilanes, *gauche* kinks significantly attenuate transmission near E_F.[7,15,16,29]

We performed density functional theory (DFT) coordinate scans to reveal the potential energy differences between **Si**[**3.3.1**] and **SiAd** of this key S−C−Si−Si dihedral in both clusters (Figure 4, see Supporting Information for more detail).[30] Figure 4a shows how we label branching oligosilane paths Si_a, Si_b, and Si_c. The coordinate scan plotted in Figure 4b is for the S−C−Si−Si_a dihedral. Figure 4b shows Newman projections of the C−Si bond, where the thiomethyl group is the most sterically imposing carbon substituent. The lowest energy conformer is dictated by which cluster bridge is the most sterically imposing to the bulky thiomethyl group in staggered geometries. In the case of **Si**[**3.3.1**], the Si_b and Si_c bridges belong to flexible ring systems whereas the Si_a bridge is rigid (Figure 4a). When the bulky SMe group is *gauche* to Si_b or Si_c, the $Si_{(b,c)}Me_2Si$ groups can rotate to relieve steric interactions via ring flipping between twist-boat and chair conformations, which lessens the energetic penalty in *gauche* $Si_{b,c}$ orientations. The rigidity of the Si_a bridge prevents the Si_aMe_2Si group from engaging in such rotations, making the Si_a bridge in **Si**[**3.3.1**] the most sterically imposing one. Our calculations support that *anti* alignment with Si_a is the global minimum geometry for **Si**[**3.3.1**], as *gauche* Si_a alignments are 0.9−1.3 kcal mol^{-1} higher in relative energy. This geometry is also found in the SCXRD structure of **Si**[**3.3.1**] in Figure 3.

Meanwhile, our calculations show the same dihedral in **SiAd** has no energetic preference between *anti* or *gauche* states. The key dimethylsilylene bridge unique to the **SiAd** structure creates this degeneracy between minima, as it tethers the former bicyclic rings from the Si[3.3.1] system together while preventing ring flipping in the Si_b and Si_c bridges. This $SiMe_2$ bridge thus induces an effective C_3 rotational symmetry about the C−Si bond in **SiAd**, removing any steric distinction between the Si_a, Si_b, or Si_c sites from the thiomethyl group's perspective. Moreover, we find the energy barrier for dihedral rotation between these staggered conformers is lower in energy for **SiAd** than it is for **Si**[**3.3.1**], likely due to ground state destabilization effects from repulsive steric interactions with the rigidified $Si_{a,b,c}$ bridges in **SiAd**. These computational results are consistent with the disordered *anti* and *gauche*-like states we observe in the SCXRD structure for **SiAd**.

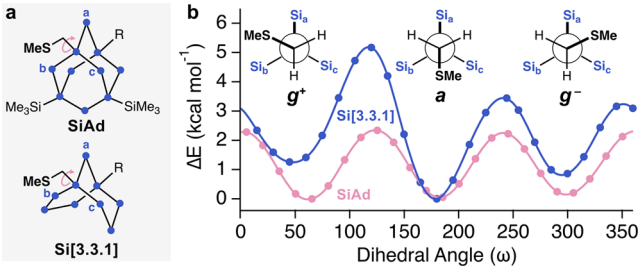

Figure 4. (a) Chemical structures of **SiAd** and **Si**[**3.3.1**]. Pink arrows denote linker dihedrals investigated in coordinate scan calculations. (**b**) Coordinate scan calculations of the S−C−Si−Si_a shown in **Figure 4a** (or S1−C2−Si1-Si2 dihedral from Figure 3) in **SiAd** and **Si**[**3.3.1**]. Each point represents a 15° rotation of the linker group, with energy plotted relative to that of the lowest energy conformer (B3LYP-D3/6−31G**). The twist-boat (Si_b path) and chair (Si_c) ring orientations in **Si**[**3.3.1**] are maintained during the coordinate scan and give two different barrier height and local minima energies. The *gauche* (**g**$^+$, **g**$^-$) and *anti* (**a**) nomenclature refers to the disposition of the thiomethyl group relative to the Si_a bridge. Newman projections shown for each local energetic minimum.

In Figure 5, we model electronic transmission through the four unique yet energetically equivalent linker-cluster rotamers of **SiAd**. We assign *anti* (**a**, $\omega \sim 180°$) and *gauche* (**g** $^{\pm}$, $\omega \sim \pm 60°$) $\omega_1\omega_2$ nomenclature based on the orientation of the two S−C−Si−Si dihedrals at each end of the molecule with the Si_a bridge. The highlighted bonds in Figure 5a depict bridges with which the linkers are anti-aligned. Using Au_{22} pyramids as proxies for electrodes, we calculate transmission through Au_{22}-**SiAd**-Au_{22} junctions using a DFT-based nonequilibrium Green's theorem approach via AITRANSS in the FHI-AIMS suite (see Supporting Information for more details).[31−33] We can rationalize conductance trends by comparing transmission values at the Fermi energy (E_F) of the gold electrodes (gray vertical line, Figure 5b); this approach is valid because our experimental measurements are executed at low voltage bias (0.1 V). While calculated transmission values at E_F do not correlate perfectly with observed conductance due to systematic errors inherent to DFT,[34−38] they are useful for rationalizing experimental conductance trends.

We find high transmission probability at E_F for the $\mathbf{a_1a_2}$ conformation when both linkers are *anti* to Si_a (Figure 5b). Its value at E_F is equivalent to what we model for **Si**[**3.3.1**] (Figure S1) and consistent with other transmission calculations of oligosilane σ-chains in the literature.[7,16] At a basic level, the high transmission of $\mathbf{a_1a_2}$ is consistent with the high HOMO energies and strong electronic coupling (Γ) between the distal S pπ pairs in *anti* backbones over *gauche* ones.[7,25,39,40] However, Figure 5b reveals an additional quantum transport facet that emerges in *gauche*-containing conformers: their transmission curves show midgap antiresonance valleys (asterisks, Figure 5b) that are signatures of destructive quantum interference (DQI) and depress transmission near E_F.[15,40,41] As these *gauche* conformers are energetically accessible for **SiAd**, their sampling in molecular junctions

https://doi.org/10.1021/jacs.5c04272
J. Am. Chem. Soc. 2025, 147, 16602−16610

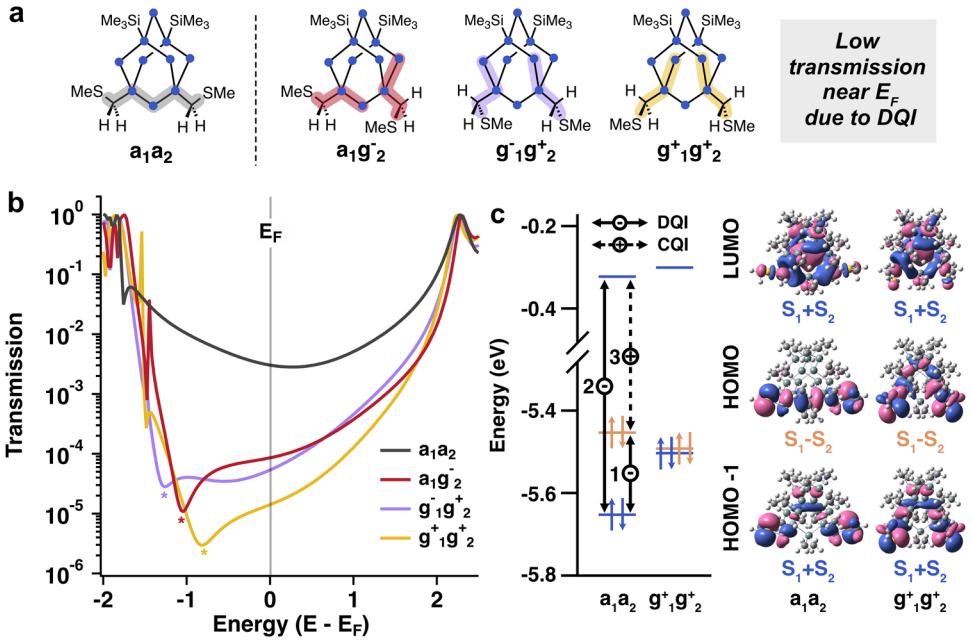

Figure 5. (a) Chemical structures of calculated **SiAd** conformers with bonds highlighted to denote which bridges the linker groups are *anti*-aligned with. (b) Transmission functions of **SiAd** conformations in Au_{22}-molecule-Au_{22} junctions obtained with AITRANSS on molecular geometries optimized via FHI-AIMS (PBE/DZ equivalent, see Supporting Information for more details). The gray line marks the Fermi energy (E_F). All *gauche* conformers show a sharp dip (*) in their transmission curves near E_F that are features of destructive quantum interference. (c) Frontier MO energies and surfaces (B3LYP-D3/6−31G**, isovalue = 0.02) of free molecule **SiAd** in $\mathbf{a_1a_2}$ and $\mathbf{g^+_1g^+_2}$ conformations as representative examples. $S_1 + S_2$ (blue) and $S_1 - S_2$ (orange) respectively denote symmetric and antisymmetric phase combinations of terminal S pπ orbitals. In the energy diagram, the dotted double-arrow line represents constructive quantum interference (CQI) interactions and solid double-arrow lines represent destructive quantum interference (DQI) interactions. DQI interactions 1 and 2 are stronger in $\mathbf{g^+_1g^+_2}$ compared to $\mathbf{a_1a_2}$.

and low transmission values rationalize the lower conductance we observe for **SiAd** compared to **Si**[**3.3.1**]. While σ-DQI effects have been described for *cisoid* ($\omega_{avg} \sim 18°$) constrained oligosilane clusters,[15,17,42,43] the present **SiAd** example is the first time σ-DQI has dominated conductance in a cluster with an *anti* bridge.

In quantum transport across molecular junctions, electrons tunnel through multiple channels (i.e., molecular orbitals) simultaneously. At a given charge carrier energy, these molecular orbitals engage in constructive quantum interference (CQI) or destructive quantum interference (DQI) with each other that leads to enhancement or attenuation of conductance, respsectively.[41,44−46] In molecules where E_F is energetically positioned between the HOMO and LUMO, interference between the frontier MOs strongly influences transmission. We can then qualitatively rationalize why DQI near E_F is stronger for *gauche* conformers by examining pairwise interference interactions between frontier MOs (HOMO−1, HOMO, LUMO) using $\mathbf{a_1a_2}$ and $\mathbf{g^+_1g^+_2}$ as representative examples (Figure 5c). We assess DQI trends by comparing the relative energies and symmetries of the interfering MOs with the following considerations:[41,44,46,,48]

First, as MO energies approach E_F, their contribution to transmission at E_F will typically increase. Relatedly, as two MOs become energetically closer to one another, the magnitude of their interference increases.

Second, the MO symmetry, and whether its energy is higher or lower than E_F, determines whether their interference is constructive or destructive at E_F with other MOs. This symmetry may be determined from the phase of the linker atom orbital that contacts the electrodes. We define S pπ contacts of the same phase as symmetric ($S_1 + S_2$, Figure 5c) and S pπ contacts of opposite phase as antisymmetric ($S_1 - S_2$). Based on this definition, we categorize the HOMO−1 and LUMO as symmetric and HOMO as antisymmetric.

Third, if the two MO energies are both below or both above E_F, they will constructively interfere at E_F if the two MOs are the same symmetry, but destructively interfere if they are opposite symmetry.[41] Meanwhile, if the energy of one MO is below E_F and the other is above it, the opposite is true, where CQI occurs between MOs of disparate symmetry, and DQI occurs between MOs of the same symmetry.

These considerations imply that the HOMO−1/HOMO interference is destructive, the HOMO−1/LUMO interference is destructive, and the HOMO/LUMO interference is constructive in **SiAd** (Figure 5c). The weakened electronic coupling between the S pπ pairs in *gauche* conformations causes the HOMO−1/HOMO energy splitting to shrink and the HOMO−1 energy to rise. As the HOMO−1 rises in energy from $\mathbf{a_1a_2}$ to $\mathbf{g^+_1g^+_2}$, destructive interference between the HOMO−1 and the HOMO (interaction 1, Figure 5c) and between the HOMO−1 and the LUMO (interaction 2, Figure 5c) should increase, lowering transmission near E_F. Meanwhile, as the HOMO energy lowers from $\mathbf{a_1a_2}$ to $\mathbf{g^+_1g^+_2}$, the constructive HOMO/LUMO interference should weaken, which also results in lower transmission near E_F. Together, these changes in interference between frontier orbitals contribute to the depressions in midgap transmission observed in Figure 5b in *gauche* orientations that give the calculated antiresonance features. Similar arguments may be used to explain why DQI strengthens and CQI weakens near E_F for the $\mathbf{a_1g^-_2}$ and $\mathbf{g^-_1g^+_2}$ conformers (Figures 5c and S5).

The same linker alignments in **Si**[**3.3.1**] similarly alter frontier MO energies (Figure S6). Indeed, if we model

https://doi.org/10.1021/jacs.5c04272
J. Am. Chem. Soc. 2025, 147, 16602−16610

transmission through the higher energy *gauche* minima of Si[3.3.1] shown in Figure 4a, we find lower transmissions near E_F (Figure S7) and in the $g^+_1g^+_2$ instance, a midgap antiresonance. Infrequent sampling of these higher energy rotamers may explain the broad, low-intensity shoulder observed at lower conductance in **Si[3.3.1]** junctions (Figure 2b). The sterically inequivalent H and SMe linker substituents and their interaction with the sterically inequivalent $Si_{a,b,c}$ bridges of **Si[3.3.1]** thus rationalize why bicyclic silanes often mirror the behavior of constrained linear oligosilanes (Figure 1b). Sila-adamantane is fundamentally distinct in this sense: because the $Si_{a,b,c}$ bridgehead branches are sterically equivalent, linker groups in the free molecule align with each cluster bridge path to equal extents, regardless of whether the linker has sterically equivalent or inequivalent substituents. The pronounced interference effects we observe in *gauche* alignments of **SiAd** are thus a defining and fundamental quantum transport trait of C_3-symmetric diamond silicon in molecular junctions.

This line of reasoning led us to hypothesize that, if we instead use sterically equivalent substituents at the linker-cluster dihedral, we could get Si[3.3.1] junctions to resemble SiAd ones by opening alignment with all bridge paths. To test this hypothesis, we synthesized two novel compounds, **SiAd-Si$_1$** and **Si[3.3.1]-Si$_1$** (Figure 6a and Scheme S1), as the methyl

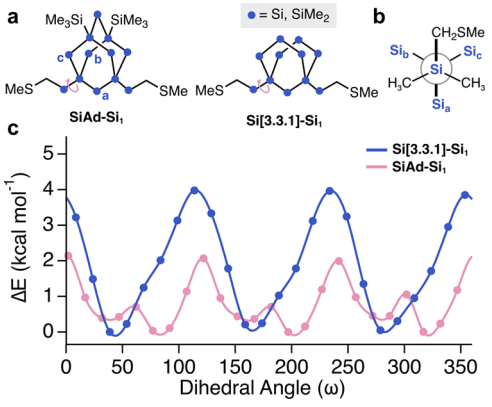

Figure 6. (a) Chemical structures of **SiAd-Si$_1$** and **Si[3.3.1]-Si$_1$**. Pink arrows denote linker dihedrals investigated in coordinate scan calculations. (**b**) Newman projection showing sterically equivalent CH_3 and CH_2SMe groups about the linker-cluster dihedral. (c) Dihedral coordinate scan calculations about the $Si_{cluster} - Si_{linker}$ bond. Each point represents a 15° dihedral rotation and its energy relative to the lowest energy conformer (B3LYP-D3/6−31G**). Two local minima are seen in each *gauche* region due to known splitting into *gauche* and *ortho* geometries due to steric interactions across permethyloligosilane chains.[50] Meanwhile, the previous *anti* geometry from Figure 4 now splits into *transoid* geometries ($\omega \pm 165°$).

(CH_3) and methylene (CH_2R) linker substituents are sterically equivalent (Figure 6b).[49] DFT scans of the linker-cluster dihedral in **SiAd-Si$_1$** and **Si[3.3.1]-Si$_1$** support this notion, as the *transoid* and *gauche*/*ortho*[50] global minima in the free molecule are essentially degenerate in energy (Figure 6c, (B3LYP-D3/6−31G**), see Supporting Information). The conductance profile of **Si[3.3.1]-Si$_1$** should thus closely resemble that of **SiAd-Si$_1$** if all cluster bridges are accessible for *anti*-like linker alignment.

Indeed, the 1D conductance histograms in Figure 7 are very similar for **SiAd-Si$_1$** and **Si[3.3.1]-Si$_1$**, as they each show a

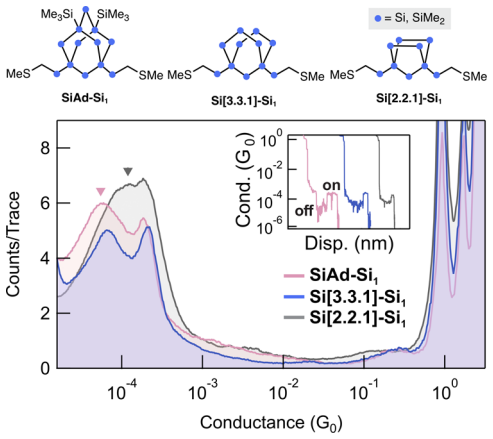

Figure 7. Overlaid 1D conductance histograms of **SiAd-Si$_1$** (red), **Si[3.3.1]-Si$_1$** (blue), and **Si[2.2.1]-Si$_1$** (gray) that compile at least 10,000 measurement traces for each molecule. All molecules were measured in 1 mM solutions in 1,2,4-trichlorobenzene at 0.1 V bias. The triangles mark the low G peak for **SiAd-Si$_1$** (pink) and **Si[2.2.1]-Si$_1$** (gray) to emphasize the prominent off-state lowering effect observed for **SiAd-Si$_1$**. Inset: Representative elongation traces for each molecule studied. These single traces show a distinct switching event from low to high G conductance ranges as the junction elongates. Most probable conductance peak values (low *G*, high *G*): **SiAd-Si$_1$** (5.92×10^{-5} G_0, 1.85×10^{-4} G_0), **Si[3.3.1]-Si$_1$** (6.72×10^{-5} G_0, 2.07×10^{-4} G_0), **Si[2.2.1]-Si$_1$** (1.59×10^{-4} G_0, 1.73×10^{-4} G_0), **Si$_5$** (1.59×10^{-4} G_0, Figure S8).

broad low conductance (*G*) peak and a narrow high *G* peak at roughly the same peak position. The low *G* peak likely corresponds to geometries with *gauche* cluster-linker dihedrals and the high *G* peak like corresponds to all-*transoid* geometries. This similarity confirms our hypothesis above: the absence of steric distinction in the linker now allows the electrodes to couple into all bridge paths of SiAd and Si[3.3.1] to appreciable extents. The presence of two clearly defined conductance peaks suggests a path toward single-molecule conductance switches, where the high and low *G* states can represent the "on" and "off" states of binary logic. The individual junction traces (inset, Figure 7) and 2D conductance histograms (Figure S8) reveal that many measurement traces begin in the low *G* state, and as the junctions are stretched, the traces jump to a high *G* state that can be sustained at longer tip-electrode displacement lengths. This behavior resembles the stereoelectronic switching behavior that was previously described for linear oligosilane junctions,[13] except that the high *G*/low *G* ratios we find here are significantly larger. We include the 1D and 2D histograms of linear **Si$_5$**[13] in Figure S8 for comparison.

DFT models of junction stretching suggest that cluster wires with -$SiMe_2CH_2SMe$ linkers displace mechanical strain via dihedral straightening from *gauche*-like to *anti*-like conformers (Figure S9), whereas cluster wires with the shorter $-CH_2SMe$ linkers cannot (Figure S9). If a **SiAd** junction begins with *gauche* linker-cluster dihedrals, these configurations are likely maintained even as the junction is stretched to its breakpoint (Figure S9). This reluctancy to switch into the all-*anti* conformation is consistent with the low **SiAd** conductance we show in Figure 2. But if the same situation occurs for **SiAd-Si$_1$**, the flexibility in the Si_1 linker allows the linker-cluster dihedral to straighten from a *gauche*/*ortho* to a *transoid* configuration upon junction stretching (Figure S9). This change in linker geometry alleviates σ-DQI between frontier

https://doi.org/10.1021/jacs.5c04272
J. Am. Chem. Soc. 2025, 147, 16602−16610

MOs and manifests as a sharp increase in junction conductance that we show in the Figure 7 inset as the junction elongates.

While Si_1 linkers have been previously appended to Si clusters, the high G/low G ratios are appreciably smaller than what we observe here. Li et al. appended Si_1 linkers to cyclosilane rings and bicyclic clusters (i.e., **Si[2.2.1]-Si$_1$**, Figure 7).[16] While all molecules in Figure 7 have the same high G value, the low G peak is roughly 2-fold lower in conductance for **SiAd-Si$_1$** and **Si[3.3.1]-Si$_1$** than it is for **Si[2.2.1]-Si$_1$** (Figure 7). DFT transmission calculations support that *gauche* cluster alignments give lower transmission near E_F for **SiAd-Si$_1$** than in **Si[2.2.1]-Si$_1$** junctions (Figure S10). This finding is exciting for single-molecule switching applications because it suggests a new design strategy based on conjugated clusters with nonequivalent bridge paths. Under this premise, an external stimulus may trigger a reversible change in the average linker alignment with the cluster bridges that would lead to a conductance switching event.

We choose to validate this concept in **SiAd-Si$_1$** in Figure 8, as it has a slightly larger high G/low G ratio than **Si[3.3.1]-Si$_1$**,

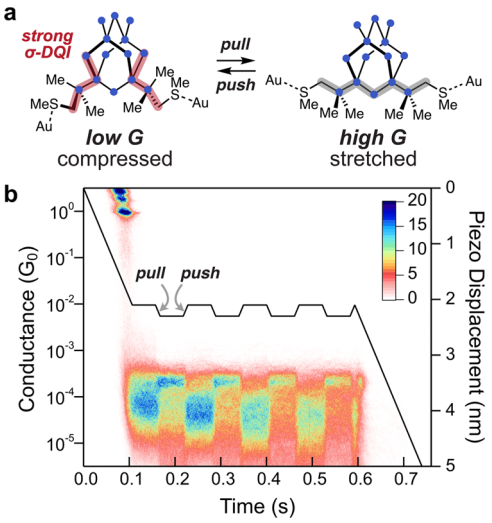

Figure 8. (a) Representative conformers of **SiAd-Si$_1$** that occur at short interelectrode distances ($g^+_1g^+_2$, *low* G "off" state) with strong σ-DQI interactions between frontier MOs and at long interelectrode distances (a_1a_2, high G "on" state) where these σ-DQI effects are relieved. (b) 2D conductance histogram of push−pull single-junction switching experiments of **SiAd-Si$_1$** in a 1 mM solution in 1,2,4-trichlorobenzene. The measurement was performed at gain 7, 100 mV, 100 kΩ, with a piezo excursion rate of 20 nm s^{-1}. 10,000 measurement traces were collected. 3,372 traces were selected based on whether the conductance registered at the beginning of the pull/push cycles was within a range of $10^{-2.5}$ to $10^{-5.5}$ G_0 (see Figure S12). The black line represents piezo displacement over the duration of a conductance trace. The piezo follows this trajectory to collect each trace: 2.1 nm initial pull, 4 cycles (0.05 s hold, 0.2 nm pull, 0.05 s hold, 0.2 nm push for each cycle), and 3.5 nm final pull.

though we note these two clusters should show similar switching behavior based on their similar histogram characteristics (Figures 7 and S8). We use mechanical force as a reversible stimulus, as the STM-BJ technique provides a sub-Ångstrom level of mechanical control.[13,51,52] When the junction is mechanically compressed, we expect to sample a broader set of linker geometries where the electrodes are *gauche* with Si_a (low G). When the junction is stretched and mechanically strained, we would expect a narrower set of geometries favoring *transoid* alignments with Si_a (high G, Figure 8). To test this experimentally, we apply a modified piezo ramp (Figure S11) where we first pull until a molecular junction forms, stretch and compress the molecular junction over four cycles by 2 Å to induce switching between high and low G states, then stretch the junction until it breaks. We performed ten thousand of these measurements. Figure 8 plots all traces where a molecule forms an initial molecular junction (See Figure S12 for trace selection criteria). We find switching is largely reversible and becomes more distinct with each cycle, mirroring the "junction training" effects described previously.[13,52] We find an average 5.6-fold switching factor between high and low G states in the final cycle (see Supporting Note S1), which is demonstrably higher than the 2.5 to 3.4-fold factors previously found for oligosilane and oligogermane switches of similar length.[13,52−54] These switching experiments show for the first time that we can dynamically control destructive σ-quantum interference between frontier MOs by influencing torsional alignment between the electrode linkers and cluster bridge paths.

CONCLUSIONS

These findings define the molecular origins for how three-dimensional crystalline silicon is distinct from linear polysilanes in the context of charge transport. The bridgehead symmetry intrinsic to diamond silicon enables electrode alignment with all cluster bridge paths in sila-adamantane, regardless of whether the linker substituents are sterically equivalent or inequivalent. This fundamental property gives rise to the strong quantum interference effects that we observe and exploit in the sila-diamondoid wires studied here.

When the electrodes *anti*-align with the longer Si_b or Si_c cluster bridges, the molecule experiences HOMO−1 destabilization that enhances destructive σ-quantum interference near the Fermi energy. This σ-DQI results in a lower experimental conductance for **SiAd** compared to its bridge-excised analog **Si[3.3.1]** and produces the midgap transmission antiresonances found in our electronic transport calculations. It is of significant interest to explore how σ-DQI between frontier orbitals is perturbed by tuning the electronics of the bridgehead substituent groups that terminate the Si_b and Si_c cluster paths.[20] These studies are ongoing in our laboratory.

The present work also reveals a new design concept for functional molecular electronics where σ-DQI is dynamically controlled. By using the longer and more flexible Si_1 linkers, we show that mechanical force can reversibly switch which bridges of the diamondoid framework the electrodes align through. The "off" state conductance lowering we show here allow us to achieve higher on/off ratios (5.6-fold) than any other reported σ-stereoelectronic switch. Our work suggests that other conjugated Si clusters with nonequivalent bridges may similarly serve as nodes that switch resistivity by toggling the bridge paths with which the electrodes align.

ASSOCIATED CONTENT

Supporting Information

The Supporting Information is available free of charge at https://pubs.acs.org/doi/10.1021/jacs.5c04272.

Additional figures; synthetic details; structural characterization; STM-BJ details; density functional theory details; and crystallography details (PDF)

https://doi.org/10.1021/jacs.5c04272
J. Am. Chem. Soc. 2025, 147, 16602−16610

Accession Codes

CCDC 2429404−2429405 contain the supplementary crystallographic data for this paper. These data can be obtained free of charge via www.ccdc.cam.ac.uk/data_request/cif, or by emailing data_request@ccdc.cam.ac.uk, or by contacting The Cambridge Crystallographic Data Centre, 12 Union Road, Cambridge CB2 1EZ, UK; fax: + 44 1223 336033.

AUTHOR INFORMATION

Corresponding Author

Timothy A. Su − *Department of Chemistry and Materials Science & Engineering Program, University of California, Riverside, California 92506, United States;* orcid.org/0000-0001-5934-3292; Email: timothys@ucr.edu

Authors

Matthew O. Hight − *Department of Chemistry, University of California, Riverside, California 92506, United States;* Present Address: Department of Chemistry, University of Liverpool, Crown Street, Liverpool L69 7ZD, United Kingdom; orcid.org/0000-0003-1482-8768

Ashley E. Pimentel − *Department of Chemistry, University of California, Riverside, California 92506, United States;* orcid.org/0009-0008-9983-8298

Timothy C. Siu − *Department of Chemistry, University of California, Riverside, California 92506, United States*

Joshua Y. Wong − *Department of Chemistry, University of California, Riverside, California 92506, United States;* Present Address: Department of Chemistry and Chemical Biology, Cornell University, Ithaca, New York 14853, United States; orcid.org/0000-0002-5702-7146

Jennifer Nguyen − *Department of Chemistry, University of California, Riverside, California 92506, United States*

Veronica Carta − *Department of Chemistry, University of California, Riverside, California 92506, United States;* orcid.org/0000-0001-8089-8436

Complete contact information is available at: https://pubs.acs.org/10.1021/jacs.5c04272

Author Contributions

[⊥]M.O.H. and A.E.P. contributed equally to this work.

Notes

The authors declare no competing financial interest.

ACKNOWLEDGMENTS

This material is based upon work supported by the Air Force Office of Scientific Research under award numbers FA9550-22-1-0404 and FA9550-23-1-0192. This work was partially supported by a Hellman Fellowship and the Cottrell Scholars Program (CS-CSA-2024-069). Computations were performed using the computer clusters and data storage resources of the UCR HPCC, which were funded by grants from NSF (MRI-2215705, MRI-1429826) and NIH (1S10OD016290-01A1).

REFERENCES

(1) Loubet, N.; Hook, T.; Montanini, P.; Yeung, C.-W.; Kanakasabapathy, S.; Guillom, M.; Yamashita, T.; Zhang, J.; Miao, X.; Wang, J.; Young, A.; Chao, R.; Kang, M.; Liu, Z.; Fan, S.; Hamieh, B.; Sieg, S.; Mignot, Y.; Xu, W.; Seo, S.-C.; Yoo, J.; Mochizuki, S.; Sankarapandian, M.; Kwon, O.; Carr, A.; Greene, A.; Park, Y.; Frougier, J.; Galatage, R.; Bao, R.; Shearer, J.; Conti, R.; Song, H.; Lee, D.; Kong, D.; Xu, Y.; Arceo, A.; Bi, Z.; Xu, P.; Muthinti, R.; Li, J.; Wong, R.; Brown, D.; Oldiges, P.; Robison, R.; Arnold, J.; Felix, N.; Skordas, S.; Gaudiello, J.; Standaert, T.; Jagannathan, H.; Corliss, D.; Na, M.-H.; Knorr, A.; Wu, T.; Gupta, D.; Lian, S.; Divakaruni, R.; Gow, T.; Labelle, C.; Lee, S.; Paruchuri, V.; Bu, H.; Khare, M. *Stacked Nanosheet Gate-All-around Transistor to Enable Scaling beyond FinFET*; 2017 Symposium on VLSI Technology; IEEE: Kyoto, Japan, 2017; pp T230−T231 DOI: 10.23919/VLSIT.2017.7998183.

(2) Wu, L. The next Generation of Gate-All-around Transistors. *Nat. Electron.* **2023**, *6* (7), 469−469.

(3) Cao, W.; Bu, H.; Vinet, M.; Cao, M.; Takagi, S.; Hwang, S.; Ghani, T.; Banerjee, K. The Future Transistors. *Nature* **2023**, *620* (7974), 501−515.

(4) Robertson, J.; Wallace, R. M. High-K Materials and Metal Gates for CMOS Applications. *Mater. Sci. Eng. R: Rep.* **2015**, *88*, 1−41.

(5) Neyens, S.; Zietz, O. K.; Watson, T. F.; Luthi, F.; Nethwewala, A.; George, H. C.; Henry, E.; Islam, M.; Wagner, A. J.; Borjans, F.; Connors, E. J.; Corrigan, J.; Curry, M. J.; Keith, D.; Kotlyar, R.; Lampert, L. F.; Mądzik, M. T.; Millard, K.; Mohiyaddin, F. A.; Pellerano, S.; Pillarisetty, R.; Ramsey, M.; Savytskyy, R.; Schaal, S.; Zheng, G.; Ziegler, J.; Bishop, N. C.; Bojarski, S.; Roberts, J.; Clarke, J. S. Probing Single Electrons across 300-Mm Spin Qubit Wafers. *Nature* **2024**, *629* (8010), 80−85.

(6) Zwanenburg, F. A.; Dzurak, A. S.; Morello, A.; Simmons, M. Y.; Hollenberg, L. C. L.; Klimeck, G.; Rogge, S.; Coppersmith, S. N.; Eriksson, M. A. Silicon Quantum Electronics. *Rev. Mod. Phys.* **2013**, *85* (3), No. 961.

(7) George, C. B.; Ratner, Ma; Lambert, J. B. Strong Conductance Variation in Conformationally Constrained Oligosilane Tunnel Junctions. *J. Phys. Chem. A* **2009**, *113* (16), 3876−3880.

(8) Su, T. A.; Li, H.; Klausen, R. S.; Kim, N. T.; Neupane, M.; Leighton, J. L.; Steigerwald, M. L.; Venkataraman, L.; Nuckolls, C. Silane and Germane Molecular Electronics. *Acc. Chem. Res.* **2017**, *50* (4), 1088−1095.

(9) Siu, T. C.; Wong, J. Y.; Hight, M. O.; Su, T. A. Single-Cluster Electronics. *Phys. Chem. Chem. Phys.* **2021**, *23* (16), 9643−9659.

(10) Xu, B.; Tao, N. J. Measurement of Single-Molecule Resistance by Repeated Formation of Molecular Junctions. *Science* **2003**, *301* (5637), 1221−1223.

(11) Venkataraman, L.; Klare, J. E.; Tam, I. W.; Nuckolls, C.; Hybertsen, M. S.; Steigerwald, M. L. Single-Molecule Circuits with Well-Defined Molecular Conductance. *Nano Lett.* **2006**, *6* (3), 458−462.

(12) Klausen, R. S.; Widawsky, J. R.; Steigerwald, M. L.; Venkataraman, L.; Nuckolls, C. Conductive Molecular Silicon. *J. Am. Chem. Soc.* **2012**, *134* (10), 4541−4544.

(13) Su, T. A.; Li, H.; Steigerwald, M. L.; Venkataraman, L.; Nuckolls, C. Stereoelectronic Switching in Single-Molecule Junctions. *Nat. Chem.* **2015**, *7* (3), 215−220.

(14) Li, H.; Garner, M. H.; Shangguan, Z.; Zheng, Q.; Su, T. A.; Neupane, M.; Li, P.; Velian, A.; Steigerwald, M. L.; Xiao, S.; Nuckolls, C.; Solomon, G. C.; Venkataraman, L. Conformations of Cyclopentasilane Stereoisomers Control Molecular Junction Conductance. *Chem. Sci.* **2016**, *7* (9), 5657−5662.

(15) Garner, M. H.; Li, H.; Chen, Y.; Su, T. A.; Shangguan, Z.; Paley, D. W.; Liu, T.; Ng, F.; Li, H.; Xiao, S.; Nuckolls, C.; Venkataraman, L.; Solomon, G. C. Comprehensive Suppression of Single-Molecule Conductance Using Destructive σ-Interference. *Nature* **2018**, *558* (7710), 416−419.

(16) Li, H.; Garner, M. H.; Shangguan, Z.; Chen, Y.; Zheng, Q.; Su, T. A.; Neupane, M.; Liu, T.; Steigerwald, M. L.; Ng, F.; Nuckolls, C.; Xiao, S.; Solomon, G. C.; Venkataraman, L. Large Variations in the Single-Molecule Conductance of Cyclic and Bicyclic Silanes. *J. Am. Chem. Soc.* **2018**, *140* (44), 15080−15088.

(17) Garner, M. H.; Li, H.; Neupane, M.; Zou, Q.; Liu, T.; Su, T. A.; Shangguan, Z.; Paley, D. W.; Ng, F.; Xiao, S.; Nuckolls, C.; Venkataraman, L.; Solomon, G. C. Permethylation Introduces Destructive Quantum Interference in Saturated Silanes. *J. Am. Chem. Soc.* **2019**, *141* (39), 15471−15476.

(18) Brus, L. Luminescence of Silicon Materials: Chains, Sheets, Nanocrystals, Nanowires, Microcrystals, and Porous Silicon. *J. Phys. Chem.* **1994**, *98* (14), 3575−3581.
(19) Fischer, J.; Baumgartner, J.; Marschner, C. Synthesis and Structure of Sila-Adamantane. *Science* **2005**, *310* (5749), No. 825.
(20) Siu, T. C.; Cardenas, M. I. A.; Seo, J.; Boctor, K.; Shimono, M. G.; Tran, I. T.; Carta, V.; Su, T. A. Site-Selective Functionalization of Sila-Adamantane and Its Ensuing Optical Effects. *Angew. Chem., Int. Ed.* **2022**, *61* (31), No. e202206877.
(21) Cardenas, M. I. A.; Siu, T. C.; Pimentel, A. E.; Hight, M. O.; Shimono, M. G.; Thai, S.; Carta, V.; Su, T. A. Installing Quaternary Germanium Centers in Sila-Diamondoid Cores via Skeletal Isomerization. *J. Am. Chem. Soc.* **2023**, *145* (37), 20588−20594.
(22) Datta, S. *Quantum Transport: Atom to Transistor*; Cambridge University Press: Cambridge New York, 2013.
(23) Zirngast, M.; Baumgartner, J.; Marschner, C. Synthesis of Cyclic and Bicyclic Polysilanes of Variable Ring Sizes. *Organometallics* **2008**, *27* (24), 6472−6478.
(24) Martin, C. A.; Ding, D.; Sørensen, J. K.; Bjørnholm, T.; Van Ruitenbeek, J. M.; Van Der Zant, H. S. J. Fullerene-Based Anchoring Groups for Molecular Electronics. *J. Am. Chem. Soc.* **2008**, *130* (40), 13198−13199.
(25) Schepers, T.; Michl, J. Optimized Ladder C and Ladder H Models for Sigma Conjugation: Chain Segmentation in Polysilanes. *J. Phys. Org. Chem.* **2002**, *15* (8), 490−498.
(26) Bande, A.; Michl, J. Conformational Dependence of σ-Electron Delocalization in Linear Chains: Permethylated Oligosilanes. *Chem. - Eur. J.* **2009**, *15* (34), 8504−8517.
(27) Jovanovic, M.; Antic, D.; Rooklin, D.; Bande, A.; Michl, J. Intuitive Understanding of σ Delocalization in Loose and σ Localization in Tight Helical Conformations of an Oligosilane Chain. *Chem. - Asian J.* **2017**, *12* (11), 1250−1263.
(28) Jovanovic, M.; Michl, J. Effect of Conformation on Electron Localization and Delocalization in Infinite Helical Chains [X(CH3)-2]∞ (X = Si, Ge, Sn, and Pb). *J. Am. Chem. Soc.* **2019**, *141* (33), 13101−13113.
(29) Pan, H.; Dong, Y.; Wang, Y.; Li, J.; Zhang, Y.; Gao, S.; Wang, Y.; Hou, S. Conformational Control of σ-Interference Effects in the Conductance of Permethylated Oligosilanes. *J. Am. Chem. Soc.* **2024**, *146* (50), 34617−34627.
(30) Frisch, M. J.; Trucks, G. W.; Schlegel, H. B.; Scuseria, G. E.; Robb, M. A.; Cheeseman, J. R.; Scalmani, G.; Barone, V.; Petersson, G. A.; Nakatsuji, H.; Li, X.; Caricato, M.; Marenich, A. V.; Bloino, J.; Janesko, B. G.; Gomperts, R.; Mennucci, B.; Hratch, D. J. *Gaussian 16*; Revision C.01; Gaussian, Inc.: Wallingford, CT, 2016.
(31) Blum, V.; Gehrke, R.; Hanke, F.; Havu, P.; Havu, V.; Ren, X.; Reuter, K.; Scheffler, M. Ab Initio Molecular Simulations with Numeric Atom-Centered Orbitals. *Comput. Phys. Commun.* **2009**, *180* (11), 2175−2196.
(32) Arnold, A.; Weigend, F.; Evers, F. Quantum Chemistry Calculations for Molecules Coupled to Reservoirs: Formalism, Implementation, and Application to Benzenedithiol. *J. Chem. Phys.* **2007**, *126* (17), No. 174101.
(33) Bagrets, A. Spin-Polarized Electron Transport Across Metal−Organic Molecules: A Density Functional Theory Approach. *J. Chem. Theory Comput.* **2013**, *9* (6), 2801−2815.
(34) Garcia-Lastra, J. M.; Rostgaard, C.; Rubio, A.; Thygesen, K. S. Polarization-Induced Renormalization of Molecular Levels at Metallic and Semiconducting Surfaces. *Phys. Rev. B* **2009**, *80* (24), No. 245427.
(35) Toher, C.; Sanvito, S. Efficient Atomic Self-Interaction Correction Scheme for Nonequilibrium Quantum Transport. *Phys. Rev. Lett.* **2007**, *99* (5), No. 056801.
(36) Quek, S. Y.; Khoo, K. H. Predictive DFT-Based Approaches to Charge and Spin Transport in Single-Molecule Junctions and Two-Dimensional Materials: Successes and Challenges. *Acc. Chem. Res.* **2014**, *47* (11), 3250−3257.
(37) Bryenton, K. R.; Adeleke, A. A.; Dale, S. G.; Johnson, E. R. Delocalization Error: The Greatest Outstanding Challenge in Density-functional Theory. *WIREs Comput. Mol. Sci.* **2023**, *13* (2), No. e1631.
(38) Buraschi, M.; Horsfield, A. P.; Cucinotta, C. S. Revealing Interface Polarization Effects on the Electrical Double Layer with Efficient Open Boundary Simulations under Potential Control. *J. Phys. Chem. Lett.* **2024**, *15* (18), 4872−4879.
(39) Tsuji, H.; Michl, J.; Tamao, K. Recent Experimental and Theoretical Aspects of the Conformational Dependence of UV Absorption of Short Chain Peralkylated Oligosilanes. *J. Organomet. Chem.* **2003**, *685* (1−2), 9−14.
(40) Su, T. A.; Neupane, M.; Steigerwald, M. L.; Venkataraman, L.; Nuckolls, C. Chemical Principles of Single-Molecule Electronics. *Nat. Rev. Mater.* **2016**, *1* (3), No. 16002.
(41) Solomon, G. C.; Andrews, D. Q.; Hansen, T.; Goldsmith, R. H.; Wasielewski, M. R.; Van Duyne, R. P.; Ratner, M. A. Understanding Quantum Interference in Coherent Molecular Conduction. *J. Chem. Phys.* **2008**, *129* (5), No. 054701.
(42) Garner, M. H.; Koerstz, M.; Jensen, J. H.; Solomon, G. C. The Bicyclo[2.2.2]Octane Motif: A Class of Saturated Group 14 Quantum Interference Based Single-Molecule Insulators. *J. Phys. Chem. Lett.* **2018**, *9* (24), 6941−6947.
(43) Garner, M. H.; Koerstz, M.; Jensen, J. H.; Solomon, G. C. Substituent Control of σ-Interference Effects in the Transmission of Saturated Molecules. *ACS Phys. Chem. Au* **2022**, *2* (4), 282−288.
(44) Lambert, C. J. Basic Concepts of Quantum Interference and Electron Transport in Single-Molecule Electronics. *Chem. Soc. Rev.* **2015**, *44* (4), 875−888.
(45) Evers, F.; Korytár, R.; Tewari, S.; Van Ruitenbeek, J. M. Advances and Challenges in Single-Molecule Electron Transport. *Rev. Mod. Phys.* **2020**, *92* (3), No. 35001.
(46) Gunasekaran, S.; Greenwald, J. E.; Venkataraman, L. Visualizing Quantum Interference in Molecular Junctions. *Nano Lett.* **2020**, *20* (4), 2843−2848.
(47) Yoshizawa, K. An Orbital Rule for Electron Transport in Molecules. *Acc. Chem. Res.* **2012**, *45* (9), 1612−1621.
(48) Cao, N.; Bro-Jørgensen, W.; Zheng, X.; Solomon, G. C. Visualizing and Comparing Quantum Interference in the π -System and σ -System of Organic Molecules. *J. Chem. Phys.* **2023**, *158* (12), No. 124305.
(49) Hight, M. O.; Wong, J. Y.; Pimentel, A. E.; Su, T. A. Intramolecular London Dispersion Interactions in Single-Molecule Junctions. *J. Am. Chem. Soc.* **2024**, *146* (7), 4716−4726.
(50) Michl, J.; West, R. Conformations of Linear Chains. Systematics and Suggestions for Nomenclature. *Acc. Chem. Res.* **2000**, *33* (12), 821−823.
(51) Quek, S. Y.; Kamenetska, M.; Steigerwald, M. L.; Choi, H. J.; Louie, S. G.; Hybertsen, M. S.; Neaton, J. B.; Venkataraman, L. Mechanically Controlled Binary Conductance Switching of a Single-Molecule Junction. *Nat. Nanotechnol.* **2009**, *4* (4), 230−234.
(52) Su, T. A.; Li, H.; Zhang, V.; Neupane, M.; Batra, A.; Klausen, R. S.; Kumar, B.; Steigerwald, M. L.; Venkataraman, L.; Nuckolls, C. Single-Molecule Conductance in Atomically Precise Germanium Wires. *J. Am. Chem. Soc.* **2015**, *137* (38), 12400−12405.
(53) These studies suggest that terminal EMe_2-EMe_2-CH_2-S (E = Si, Ge) dihedrals are likely more important in the stereoelectronic conductance switching of silane and germane wires than we had previously appreciated, supporting recent conclusions by Solomon and co-workers (ref 54.).
(54) Hamill, J. M.; Bro-Jørgensen, W.; Balogh, Z.; Li, H.; Leitherer, S.; Solomon, D.; Halbritter, A.; Solomon, G. Improving Single-Molecule Conductance Measurements with Change Point Detection from the Econometrics Toolbox, 2024. arXiv:2401.12769. arXiv.org e-Printarchive. https://doi.org/10.48550/arXiv.2401.12769.